



Technical note: Measurement of chemically resolved volume equivalent diameter and effective density of particles by AAC-SPAMS

Long Peng^{1,2}, Lei Li⁴, Guohua Zhang^{1,3}, Xubing Du⁴, Xinming Wang^{1,3}, Ping'an Peng^{1,3}, Guoying Sheng¹, and Xinhui Bi^{1,3}

¹State Key Laboratory of Organic Geochemistry and Guangdong Provincial Key Laboratory of Environmental Protection and Resources Utilization, Guangzhou Institute of Geochemistry, Chinese Academy of Sciences, Guangzhou 510640, China

²University of Chinese Academy of Sciences, Beijing 100049, China

³Guangdong-Hong Kong-Macao Joint Laboratory for Environmental Pollution and Control, Guangzhou 510640, China

⁴Institute of Mass Spectrometer and Atmospheric Environment, Jinan University, Guangzhou 510632, China

Correspondence: Xinhui Bi (bixh@gig.ac.cn) and Guohua Zhang (zhanggh@gig.ac.cn)

Received: 7 October 2020 – Discussion started: 26 October 2020

Revised: 26 February 2021 – Accepted: 2 March 2021 – Published: 12 April 2021

Abstract. Size and effective density (ρ_e) are important properties of aerosol particles and are related to their influences on human health and the global climate. The volume equivalent diameter (D_{ve}) is an intrinsic property that is used to evaluate particle size. Three definitions of ρ_e are generally used to characterize the physical property of a particle as an alternative to particle density, in which only the ρ_e^{II} , defined as the ratio of particle density (ρ_p) to a dynamic shape factor (χ), has the characteristic of being independent of particle size. However, it is still challenging to simultaneously characterize the D_{ve} and ρ_e^{II} of aspherical particles. Here, we present a novel system that classifies particles with their aerodynamic diameter (D_a) by aerodynamic aerosol classifier (AAC) and determines their vacuum aerodynamic diameter (D_{va}) by single-particle aerosol mass spectrometry (SPAMS) to achieve a measurement of D_{ve} and ρ_e^{II} . The reliability of the AAC-SPAMS system for accurately obtaining D_{ve} and ρ_e^{II} is verified based on the result that the deviation between the measured and theoretical values is less than 6% for the size-resolved spherical polystyrene latex (PSL). The AAC-SPAMS system was applied to characterize the D_{ve} and ρ_e^{II} of $(\text{NH}_4)_2\text{SO}_4$ and NaNO_3 particles, suggesting that these particles are aspherical and their ρ_e^{II} is independent of particle size. Finally, the AAC-SPAMS system was deployed in a field measurement, showing that it is a powerful technique to characterize the chemically resolved D_{ve} and ρ_e^{II} of particles in real time.

1 Introduction

Size and particle density (ρ_p) are critical parameters of aerosol particles in quantifying the impact of aerosols on air quality, human health and global climate change (Buseck and Posfai, 1999; Pöschl, 2005; Pitz et al., 2003). Effective density (ρ_e) has been adopted to characterize the physical property of a particle as an alternative to ρ_p , since ρ_p for aspherical aerosol particles is hardly measured (Sumlin et al., 2018; Katrib et al., 2005). Size and ρ_e govern the transport properties of a particle both in the atmosphere and in the human respiratory system (Seinfeld and Pandis, 1998; Liu and Daum, 2008) and directly and/or indirectly influence the potential of the particle to absorb or reflect solar radiation (Tang, 1997; Zhao et al., 2019; Liu and Daum, 2008). ρ_e can also provide information concerning particle morphology (Yon et al., 2015) and serve as a tracer for atmospheric processing (Guo et al., 2014; Yin et al., 2015; Liu et al., 2015). However, the quantitative relationship between aerosol properties, namely size and ρ_e , and their effects on air quality, human health, and global climate change are not yet well understood, which is partly because important aerosol properties cannot be measured by current techniques.

1.1 Size

Size is a fundamental property of particles and can be parameterized by the physical quantity of volume equivalent diameter (D_{ve}). Defined as the diameter of a spherical particle with the same volume as the particle (DeCarlo et al., 2004), D_{ve} is an intrinsic physical quantity that can be used to evaluate the actual size of the particle. However, to date, atmospheric science usually describes particle size by other diameter definitions, such as the electric mobility diameter (D_m), aerodynamic equivalent diameter (D_a), and vacuum aerodynamic equivalent diameter (D_{va}), whose relationships with D_{ve} are shown in Eqs. (1)–(3), respectively:

$$\frac{D_m}{C_c(D_m)} = \frac{D_{ve}}{C_c(D_{ve})} \chi_t, \quad (1)$$

$$D_a = D_{ve} \sqrt{\frac{\rho_p C_c(D_{ve})}{\chi_t \cdot \rho_0 \cdot C_c(D_a)}}, \quad (2)$$

$$D_{va} = \frac{\rho_p}{\rho_0} \frac{D_{ve}}{\chi_v}, \quad (3)$$

where $C_c(D)$ is the Cunningham slip correction factor, χ_t and χ_v represent the aerosol dynamic shape factor (χ) in the transition regime and in the free-molecule regime, respectively, and ρ_0 represents the unit density of 1.0 g/cm^3 . From these definitions, it can be seen that D_m , D_a , and D_{va} are originally derived from D_{ve} , but in actuality they do not reflect the actual size of the aspherical particle. Meanwhile, D_{ve} of aspherical particles cannot be easily obtained, which limits its application in the scientific community.

1.2 Effective density

At present, three definitions of ρ_e are introduced in atmospheric science (DeCarlo et al., 2004): the first definition (ρ_e^I) is the ratio of the measured particle mass (m_p) to the particle volume (V) calculated assuming a spherical particle with a diameter equal to the measured D_m , the second definition (ρ_e^{II}) is the ratio of ρ_p to χ (Hand and Kreidenweis, 2002), and the third definition (ρ_e^{III}) is the ratio of D_m and D_{va} , expressed in Eqs. (4)–(6), respectively.

$$\rho_e^I = \frac{6m_p}{\pi D_m^3}, \quad (4)$$

$$\rho_e^{II} = \frac{\rho_p}{\chi}, \quad (5)$$

$$\rho_e^{III} = \frac{D_{va}}{D_m} \rho_0. \quad (6)$$

The definitions of ρ_e^I and ρ_e^{III} can be derived into their final forms, as shown in the Eqs. (7) and (8), respectively.

$$\rho_e^I = \frac{\rho}{\chi_t^3} \cdot \left(\frac{C_c(D_{ve})}{C_c(D_m)} \right)^3 \quad (7)$$

$$\rho_e^{III} = \rho \cdot \frac{C_c(D_{ve})}{\chi^2 \cdot C_c(D_m)} \quad (8)$$

Equation (7) is derived from combining Eq. (1) with Eq. (4), in which m_p is equal to $1/6\rho \cdot D_{ve}^3$. The detailed derivation of Eq. (8) is presented in Schneider et al. (2006). A variety of methods are developed to characterize ρ_e^I and ρ_e^{III} , among which the more advanced methods are to achieve the measurement of the chemically resolved effective density. Combining a single-particle soot photometer (SP2) with a (volatility) tandem differential mobility analyzer ((VT)DMA) can measure the ρ_e^I of particles mixed with soot (Y. Zhang et al., 2016; Wu et al., 2019; Han et al., 2019). The measurement of chemically resolved ρ_e^{III} can be achieved by coupling a DMA with an online aerosol mass spectrometer such as the Single-Particle Laser Ablation Time-of-Flight Mass Spectrometer (SPLAT) (Zelenyuk et al., 2005, 2006; Alexander et al., 2016), aerosol mass spectrometer (AMS) (Dinar et al., 2006; Schneider et al., 2006; Kiselev et al., 2010), aerosol time-of-flight mass spectrometer (ATOFMS) (Spencer and Prather, 2006; Spencer et al., 2007), and single-particle aerosol mass spectrometry (SPAMS) (G. Zhang et al., 2016; Zhai et al., 2017). However, the ρ_e^I and ρ_e^{III} are demonstrated to have the inherent characteristic of decreasing with increasing particle size, which will be presented in a separate publication. Therefore, it will introduce systemic error when assessing the particle's impact on visibility, human health, and climate change from the physical quantities in ρ_e^I and ρ_e^{III} . In contrast, ρ_e^{II} is independent of particle size. For example, for soot particles with χ of 2.5 and ρ_p of 1.80 g/cm^3 , the calculated ρ_e^I , ρ_e^{II} , and ρ_e^{III} are 0.43, 0.72, and 0.45 g/cm^3 at D_m of 40 nm and 0.22, 0.72, and 0.36 g/cm^3 at D_m of 550 nm, respectively. The big gap between the three definitions of effective density suggests that they should be carefully treated when characterizing the particles. However, the ρ_e^{II} has not been widely applied in atmospheric sciences because of the lack of measurement techniques. Previous literature has tried to retrieve the ρ_e^{II} and the real part in the refractive index (n) through a fitting procedure that compares the measured light-scattering intensity of particles (R_{meas}) to the theoretical values ($R_{theory,test}$) calculated by a series of n and ρ_e^{II} values (Moffet and Prather, 2005; Moffet et al., 2008; G. Zhang et al., 2016). Moffet and Prather (2005) successfully obtained ρ_e^{II} for spherical particles via single-particle mass spectrometry. However, subject to the accuracy of Mie theory for the aspherical particles, dry NaCl and calcium-rich dust particles failed to fit the $R_{theory,test}$ well to R_{meas} (Moffet et al., 2008). Similarly, G. Zhang et al. (2016) failed to simultaneously retrieve ρ_e^{II} and n for $(\text{NH}_4)_2\text{SO}_4$ and NaNO_3 particles. To the best of our knowledge, there is no appropriate technique to achieve the measurement of ρ_e^{II} for aspherical particles.

The aim of the present work is to develop a method to simultaneously obtain D_{ve} and ρ_e^{II} for aspherical particles. For simplicity, the symbol ρ_e in the following text refers to the definition of ρ_e^{II} . The established system of aerodynamic aerosol classifier single-particle aerosol mass spectrometry (AAC-SPAMS) is capable of characterizing the D_a and D_{va}

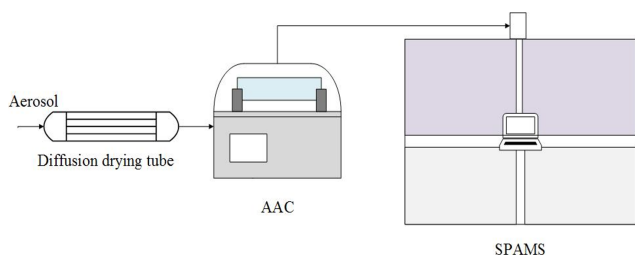


Figure 1. Schematic diagram of the AAC-SPAMS system (0.3 L/min). The diffusion drying tube is filled with orange silica gel, which reduces the RH to 5%–15%.

of particles, which can be applied to theoretically derive D_{ve} and ρ_e . To verify the reliability of the AAC-SPAMS system, we apply it to measure the D_{ve} and ρ_e of the spherical particles of polystyrene latex (PSL). The results are in good agreement with the theoretical values. Finally, the AAC-SPAMS system is applied to measure the D_{ve} and ρ_e for $(\text{NH}_4)_2\text{SO}_4$ and NaNO_3 particles and for the chemically resolved atmospheric particles.

2 Experimental section

2.1 Measurement system

Figure 1 shows a schematic diagram of the AAC-SPAMS system. The particles are first dried by a diffusion drying tube (TSI 9302, USA), classified by AAC (Cambustion Ltd., UK) based on the D_a , and then transported into SPAMS, where the D_{va} and the mass spectra of individual particles are obtained. The working principle of the AAC is described in detail elsewhere (Tavakoli and Olfert, 2013). AAC consists of two coaxial cylinders that rotate at the same rotational speed. Polydisperse particles enter into the space between the cylinders (i.e., the classification column) and experience a centrifugal force that causes them to move toward the outer cylinder. The particles to be classified can leave the classification column with the particle-free sheath flow and finally exit the AAC with the sample flow. Thus, the D_a values of classified particles can be derived from their relationship with their relaxation time (τ), as shown in Eq. (9):

$$\tau = \frac{C_c(D_a) \cdot \rho_0 \cdot D_a^2}{18\mu}, \quad (9)$$

where μ is the gas dynamic viscosity. Particles with large relaxation times impact and adhere to the outer cylinder, while particles with small relaxation times exit the classifier with the exhaust flow. In this study, the exhaust flow from the AAC was about 0.3 L/min, and the size resolution parameter of the AAC was set as 40.

Detailed information about the operation of SPAMS (Hexin Analytical Instrument Co., Ltd., China) is given elsewhere (Li et al., 2011). Briefly, the particles are introduced

into the vacuum system through a 0.1 mm critical orifice and are gradually collimated into a beam in the aerodynamic lens. Two continuous diode Nd:YAG laser beams (532 nm) are used to aerodynamically size the particles, which are subsequently desorbed and ionized by a pulsed laser (266 nm) that is triggered based on the velocity of a specific particle. The generated positive and negative ions are recorded with the corresponding particle size. The D_{va} of the particle is related to the transit time between the two laser beams (532 nm) in SPAMS, which can be obtained by using a calibration curve generated from the measured transit times of a PSL series with predefined sizes (nominal diameters).

2.2 Laboratory experiments

Dried spherical PSL (Nanosphere Size Standards, Duke Scientific Corp., Palo Alto) ($\rho_p = 1.055 \text{ g/cm}^3$ and $\chi = 1.0$) with D_{ve} values of 203 ± 5 , 310 ± 6 , 510 ± 5 , and $740 \pm 6 \text{ nm}$ were used in the AAC-SPAMS system, and the D_{ve} was verified by Scanning Mobility Particle Sizer (Model 3938, TSI Inc., USA). The PSL particles were first classified by AAC, and then their D_{va} values were obtained by SPAMS. AAC-SPAMS was also applied to the particles of $(\text{NH}_4)_2\text{SO}_4$ ($\rho_p = 1.77 \text{ g/cm}^3$) and NaNO_3 ($\rho_p = 2.26 \text{ g/cm}^3$) with D_a values of 250.0, 350.0, 450.0, and 550.0 nm. Besides, to obtain the measurement uncertainty of the AAC, the D_a values of these PSL particles were measured to be 212.8 ± 0.2 , 324.7 ± 0.4 , 529.9 ± 0.4 , and 767.5 ± 0.4 by the system of AAC condensation particle counter (CPC), respectively. It shows that the AAC has the deviations of 1.1%, 1.3%, 0.8%, and 0.7% for determining the D_a values of the particles.

2.3 Ambient sampling

For field observations, the AAC-SPAMS system was deployed in Science and Technology Enterprise Accelerator A2 Block, Guangzhou, China, to characterize the D_{ve} , ρ_e , and chemical compositions of aerosol particles. The sampling inlet was hung 2.5 m from the third floor ($\sim 12 \text{ m}$ above ground level). Ambient aerosol particles were introduced into the AAC through a 5 m long conductive silicone tube with an inner diameter of 6 mm and a $\text{PM}_{2.5}$ cyclone inlet. The sampling flow from the $\text{PM}_{2.5}$ cyclone inlet was 3 L/min, and the residence time in the conductive silicone tube was approximately 5 s. Particles with the D_a of 250.0, 350.0, 450.0, and 550.0 nm were classified by the AAC. The sampling time for the particles of each D_a was approximately 10 min. From 6–8 July 2019, approximately 129 869 ionized particles were obtained from nine rounds of measurement. The sampling details are shown in Table S1 in the Supplement. The number of ionized particles with the D_a of 250.0, 350.0, 450.0, and 550.0 nm is 35 609, 38 374, 31 910, and 23 976, respectively. The sampled $\sim 100\,000$ particles are first classified by using an adaptive resonance theory neural network (ART-2a)

(Song et al., 1999) with a vigilance factor of 0.75, a learning rate of 0.05, and 20 iterations.

2.4 Theoretical derivation of D_{ve} and ρ_e from D_a and D_{va}

In this study, the calculations of D_{ve} and ρ_e for unknown particles are theoretically derived from D_a and D_{va} . Combining Eqs. (2) and (3), we obtain Eq. (10):

$$C_c(D_a) \frac{D_a^2}{D_{va}} = D_{ve} C_c(D_{ve}) \frac{\chi_v}{\chi_t}. \quad (10)$$

Based on the approximation between χ_v and χ_t ($\chi_v \approx \chi_t = \chi_a$) (DeCarlo et al., 2004), Eq. (10) becomes Eq. (11):

$$C_c(D_a) \frac{D_a^2}{D_{va}} = D_{ve} C_c(D_{ve}). \quad (11)$$

The Cunningham slip correction factor is calculated by Eq. (12) (Peng and Bi, 2020):

$$C_c(D) = 1 + \frac{\lambda}{D} \left(A + B \cdot \exp\left(\frac{C \cdot D}{\lambda}\right) \right), \quad (12)$$

where λ is the mean free path of the gas molecules and A , B , and C are empirically determined constants specific to the analysis system. The values of A , B , and C are 2.33, 0.966, and -0.498 provided by the manual of the AAC, respectively. Substituting Eq. (12) into Eq. (11) obtains Eq. (13):

$$\begin{aligned} \frac{D_a^2}{D_{va}} + \frac{D_a \cdot \lambda}{D_{va}} \left(A + B \cdot \exp\left(\frac{C \cdot D_a}{\lambda}\right) \right) \\ = D_{ve} + \lambda \left(A + B \cdot \exp\left(\frac{C \cdot D_{ve}}{\lambda}\right) \right) \end{aligned} \quad (13)$$

If the D_a and D_{va} of an unknown particle can be measured, its D_{ve} could be calculated according to Eq. (13). Finally, the ρ_e value of the particles is calculated by the D_{va} and D_{ve} values according to Eq. (14), which is obtained by combining Eqs. (3) and (5):

$$\rho_e = \frac{\rho_p}{\chi_a} = \frac{D_{va}}{\rho_0 \cdot D_{ve}}. \quad (14)$$

Thus, we can obtain both the D_{ve} and ρ_e values of unknown particles based on the D_a and D_{va} values. Because the AAC and SPAMS instruments have the ability to determine D_a and D_{va} , the AAC-SPAMS system developed in this study can be used to obtain the D_{ve} and ρ_e values for unknown particles.

3 Results and discussion

3.1 Verification of the AAC-SPAMS system to obtain D_{ve} and ρ_e

The D_{va} distribution of PSL particles with predefined D_{ve} values after being screened by the AAC is shown in Fig. S1

in the Supplement. Gaussian fitting is used to obtain the peak D_{va} for each size PSL with R^2 fitting coefficient over 0.98. Each fitting has a full width at half maximum (FWHM) of 6.6 %, 4.4 %, 2.3 %, and 2.2 %, and the corresponding peaks are 215.8, 319.0, 532.1, and 803.5 nm, respectively. Substituting the D_a and D_{va} values of PSL into Eq. (11), the measured D_{ve} ($D_{ve,me}$) of PSL from the AAC-SPAMS system is 203.6, 309.7, 511.6, and 737.2 nm, respectively (Fig. 2a). Thus, the deviations between the theoretical D_{ve} ($D_{ve,th}$) and $D_{ve,me}$ values are 0.3 %, -0.1 %, 0.3 %, and -0.4 %, respectively. On the other hand, the measured ρ_e ($\rho_{e,me}$) values of the particles, calculated from the D_{va} and $D_{ve,me}$ values with Eq. (14), are 1.1, 1.0, 1.0, and 1.1 g/cm³, respectively (Fig. 2b). Comparing to the theoretical ρ_e ($\rho_{e,th}$) (i.e., 1.055 g/cm³ of PSL particles), the deviations of $\rho_{e,me}$ are determined to be 4.3 %, -5.2 %, -5.2 %, and 4.3 %, respectively. That is, the deviations of $D_{ve,me}$ and $\rho_{e,me}$ obtained by the AAC-SPAMS system are within 1 % and 6 %, respectively.

3.2 Application of the AAC-SPAMS system for obtaining D_{ve} and ρ_e of $(\text{NH}_4)_2\text{SO}_4$ and NaNO_3

Figure S2 shows the D_{va} distributions of $(\text{NH}_4)_2\text{SO}_4$ and NaNO_3 particles with D_a values of 250.0, 350.0, 450.0, and 550.0 nm screened by the AAC. The D_{va} peaks are obtained by Gaussian fitting, with R^2 values over 0.93 and FWHM values ranging from 7.6 % to 10.6 %. The $(\text{NH}_4)_2\text{SO}_4$ particles have D_{va} values of 300.0, 418.0, 551.1, and 695.1 nm (Fig. S2), which correspond to particles possessing $D_{ve,me}$ values of 177.3, 254.4, 331.8, and 409.3 nm, respectively, according to Eq. (11). Substituting the values of D_{va} and $D_{ve,me}$ into Eq. (12), the $\rho_{e,me}$ values are 1.7, 1.6, 1.6, and 1.7 g/cm³ (Fig. 3a), respectively. Similarly, the selected NaNO_3 particles are determined to have D_{va} values of 321.0, 454.9, 599.8, and 755.3 nm (Fig. S2), corresponding to $D_{ve,me}$ values of 150.1, 218.2, 287.0, and 355.9 nm, respectively. The $\rho_{e,me}$ values of the NaNO_3 particles are 2.2, 2.0, 2.0, and 2.1 g/cm³ (Fig. 3b), respectively. Figure 3 also shows that the $\rho_{e,me}$ values of the NaNO_3 and $(\text{NH}_4)_2\text{SO}_4$ particles with different D_a deviate from their average values with the maximum of 5.9 % and 4.8 %, respectively, which are identical with the deviation for the $\rho_{e,me}$ of PSL particles. These deviations may be derived from the calibration of particle D_{va} from the SPAMS. While the R^2 of size calibration curve is 0.999, the curve of exponential function is found to slightly deviate from the data points measured by SPAMS. For example, the size calibration function produces the deviation of -4.4 % and 3.1 % from the data points of 310 and 740 nm, respectively.

Taking the systematic error into account, the slight difference of the $\rho_{e,me}$ values for the four sizes suggests that the ρ_e of $(\text{NH}_4)_2\text{SO}_4$ and NaNO_3 particles is independent of particle size from 250.0 to 550.0 nm. It is determined by the definition of effective density used in this study, which

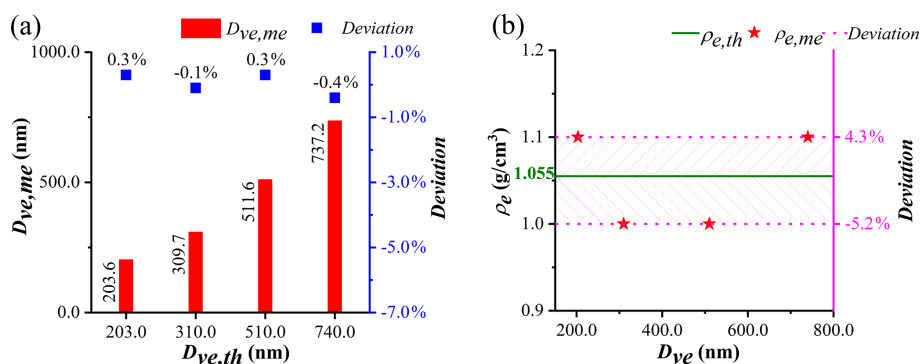


Figure 2. (a) Comparison between the measured D_{ve} ($D_{ve,me}$) and the theoretical D_{ve} ($D_{ve,th}$) of the PSL particles. (b) Comparison between the measured ρ_e ($\rho_{e,me}$) and the theoretical ρ_e ($\rho_{e,th}$) of the PSL particles.

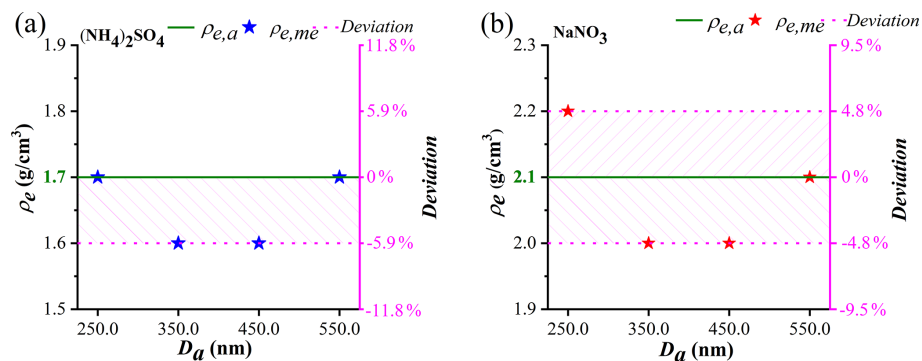


Figure 3. (a) Comparison between the measured ρ_e ($\rho_{e,me}$) and average ρ_e ($\rho_{e,a}$) values of the $(\text{NH}_4)_2\text{SO}_4$ particles. (b) Comparison between the measured ρ_e ($\rho_{e,me}$) and average ρ_e ($\rho_{e,a}$) values of the NaNO_3 particles.

keeps constant as long as the χ_a of the particles does not change with particle size for pure compound. The average $\rho_{e,me}$ values of $(\text{NH}_4)_2\text{SO}_4$ and NaNO_3 particles are calculated to be 1.7 ± 0.1 and 2.1 ± 0.1 g/cm³, which are lower than the ρ_p of $(\text{NH}_4)_2\text{SO}_4$ (1.77 g/cm³) and NaNO_3 (2.27 g/cm³). This is partly caused by the χ_a , which can be used to parameterize the morphology. According to Eq. (14), the χ_a with different D_a are calculated to be 1.04, 1.11, 1.11, and 1.04 for $(\text{NH}_4)_2\text{SO}_4$ particles and 1.03, 1.14, 1.14, and 1.08 for NaNO_3 particles. Thus, the average χ_a values of the $(\text{NH}_4)_2\text{SO}_4$ and NaNO_3 particles are determined to be 1.07 ± 0.04 and 1.10 ± 0.05 , respectively, indicating that these particles are aspherical.

The asphericity of $(\text{NH}_4)_2\text{SO}_4$ determined by AAC-SPAMS system is consistent with the previous studies reporting that the χ_a of $(\text{NH}_4)_2\text{SO}_4$ were larger than the value of 1.03 (Zelenyuk et al., 2006; Beranek et al., 2012; G. Zhang et al., 2016). However, previous studies found that the NaNO_3 particles had different morphology. G. Zhang et al. (2016) observed that NaNO_3 had the χ_a of 1.09–1.13, while Hoffman et al. (2004) found that NaNO_3 particle had a round droplet-like shape even at 15% RH, supported by the consistency between the measured value of “anhydrous” droplet density and the calculated value of “anhydrous” so-

lution droplet (Zelenyuk et al., 2005). Eclectically, Tang and Munkelwitz (1994) studied that most of the NaNO_3 particles crystallized between 20% and 30% RH but some persisted down to 10% RH to keep solution droplets. Notably, the spherical NaNO_3 particles at low RH observed by Hoffman et al. (2004) were dried in the sticky carbon tape, which might affect the phase transition of droplet-like NaNO_3 particles. In this study, most NaNO_3 particles might crystallize because the RH of the aerosol flow carrying the NaNO_3 particles was reduced to below 20% through the diffusion drying tube. The asphericity of the crystallized NaNO_3 particles is supported by their FWHM values of the D_{va} distributions, which are consistent with that of aspherical $(\text{NH}_4)_2\text{SO}_4$ (Figs. S1 and S2).

3.3 Application of the AAC-SPAMS system for measuring the chemically resolved D_{ve} and ρ_e

SPAMS can obtain information on the chemical composition of individual particles, implying that the AAC-SPAMS system has the ability to simultaneously characterize D_{ve} , ρ_e , and the chemical compositions of particles in real time. It is worth noting that the freshly emitted soot particles exhibit the largest χ (~ 2.5) in the actual atmosphere (Peng et al., 2016).

Table 1. The measured mean D_{ve} and its standard deviation for the eight particle types at D_a values of 250.0, 350.0, 450.0, and 550.0 nm from nine rounds of measurements.

D_a (nm)	K-rich	EC-S	K-Na	Amine
250.0	193.1 ± 8.2	192.2 ± 8.1	193.8 ± 21.9	190.6 ± 4.6
350.0	284.0 ± 28.4	280.8 ± 9.3	271.9 ± 18.0	284.8 ± 18.2
450.0	364.7 ± 21.1	357.8 ± 6.9	342.5 ± 7.3	367.9 ± 9.7
550.0	416.6 ± 28.3	439.5 ± 5.4	397.3 ± 29.7	442.5 ± 7.4
D_a (nm)	EC-N-S	OC-N-S	OC-EC-N-S	Metal-rich
250.0	188.5 ± 5.9	200.8 ± 17.9	195.4 ± 8.9	189.0 ± 6.7
350.0	281.3 ± 9.3	295.7 ± 29.8	294.0 ± 32.3	277.0 ± 9.1
450.0	358.0 ± 5.8	398.3 ± 44.3	428.9 ± 24.0	342.9 ± 10.0
550.0	453.2 ± 16.4	547.4 ± 14.7	570.9	407.4 ± 14.5

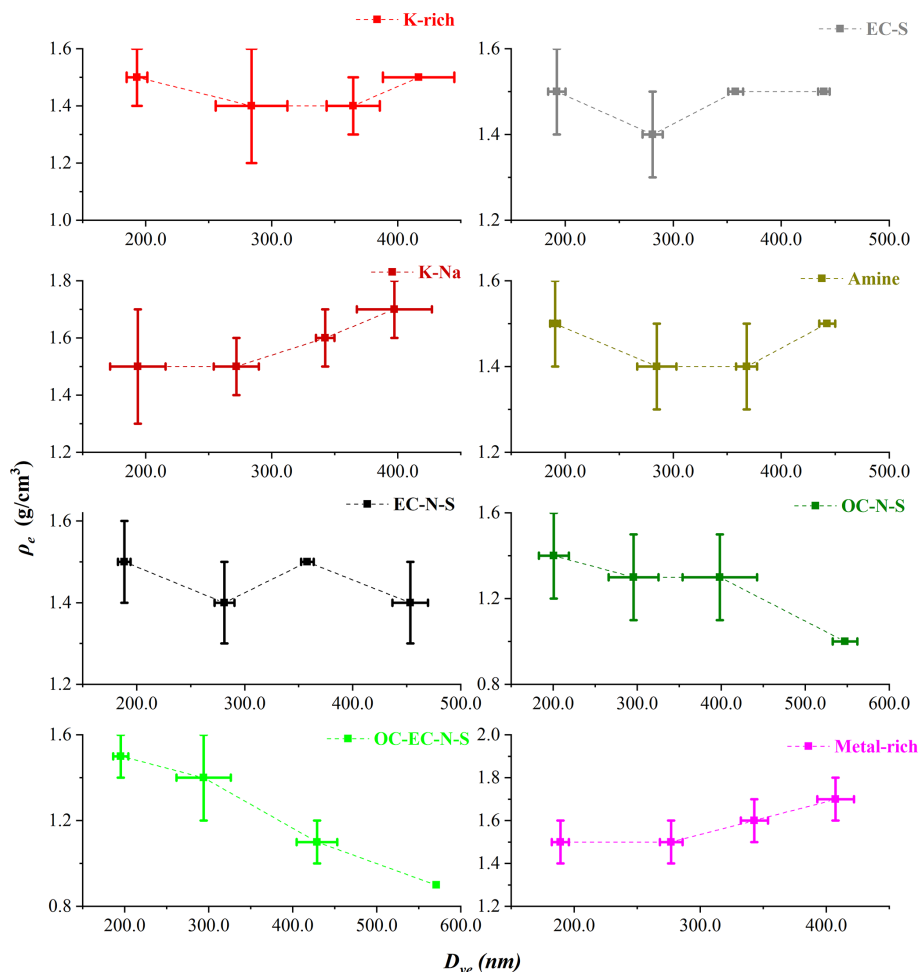


Figure 4. Variation in ρ_e of the eight particle types with D_{ve} . The solid lines represent the range of the ρ_e and D_{ve} measured from nine rounds, and the data points stand for the average values.

It meets the upper limit for the approximation between the χ_t and χ_v (DeCarlo et al., 2004).

As an example, the AAC-SPAMS system was deployed in the field to obtain the chemically resolved D_{ve} and ρ_e values for unknown aerosol particles. The sampled $\sim 100\,000$ particles are classified into eight major particle types with distinct chemical compositions: K-rich, EC-S, K-Na, amine, EC-N-S, OC-N-S and OC-EC-N-S, and Metal-rich, representing 97 % of the detected particle population. Details of the chemical composition and number fraction of the eight types of particles are presented in the Figs. S3 and S4, respectively, which are discussed in the Supplement.

We used Gaussian fitting to obtain the D_{va} peaks for each particle type with D_a values of 250.0, 350.0, 450.0, and 550.0 nm. Following this, we calculated the D_{ve} values of the atmospheric particles with Eq. (11). Table 1 presents the average D_{ve} values of the eight particle types, for which the standard deviation is calculated based on nine samples. The average D_{ve} at D_a values of 250.0, 350.0, 450.0, and 550.0 nm shows wide ranges: from 188.5 to 200.8, 271.9 to 295.7, 342.5 to 428.9, and 397.3 to 570.9 nm, respectively, which are caused by the different chemical composition. The result indicates that particles with significantly different D_{ve} might possess the same D_a . Furthermore, the large standard deviation of D_{ve} , such as 21.9 nm for K-Na at 250.0 nm, 32.3 nm for OC-EC-N-S at 350.0 nm, and 44.3 nm for OC-N-S at 450.0 nm, indicates that the D_{ve} of particles is remarkably different even for particles with the same type and same D_a .

According to D_{ve} and D_{va} , we calculated the ρ_e of each particle type by Eq. (12). Figure 4 shows the variations of the ρ_e with D_{ve} for nine particle samples. For pure compounds, such as $(\text{NH}_4)_2\text{SO}_4$ and NaNO_3 particle, ρ_e theoretically does not change with particle size. However, the sampled particles have experienced complex atmospheric processes. Therefore, ρ_e has a very wide distribution for each type of particles with a similar D_{ve} . Specifically, the ρ_e of K-Na increases with D_{ve} , while the ρ_e of OC-N-S and OC-EC-N-S decreases with D_{ve} , which may be influenced by the particle shape or the material density. Additionally, the average ρ_e of each type of particle is in the order from small to large: $1.2 \pm 0.2 \text{ g/cm}^3$ for OC-EC-N-S, $1.3 \pm 0.2 \text{ g/cm}^3$ for OC-N-S, $1.4 \pm 0.1 \text{ g/cm}^3$ for K-rich, $1.4 \pm 0.1 \text{ g/cm}^3$ for amine, $1.5 \pm 0.1 \text{ g/cm}^3$ for EC-N-S, $1.5 \pm 0.1 \text{ g/cm}^3$ for EC-S, $1.6 \pm 0.1 \text{ g/cm}^3$ for K-Na, and $1.6 \pm 0.1 \text{ g/cm}^3$ for Metal-rich. It is reasonable to find that the average ρ_e of internally mixed particles distributes in the range of their material densities (ρ_m). For instance, the OC-EC-N-S, OC-N-S, K-rich, and amine particles, mainly comprised of internally mixed sulfate and organics, have the average ρ_e between that of sulfate with ρ_m of 1.77 g/cm^3 and organic aerosols with ρ_m of 1.2 g/cm^3 (Cross et al., 2007).

4 Conclusion

We develop an AAC-SPAMS system to first achieve the measurement of the D_{ve} and ρ_e (defined as the ratio of ρ_p to χ) of the aspherical particles through characterizing their D_a and D_{va} . The reliability of the AAC-SPAMS system is verified by accurately measuring the D_{ve} and ρ_e of PSL. Applying the AAC-SPAMS system to determine the D_{ve} and ρ_e of $(\text{NH}_4)_2\text{SO}_4$ and NaNO_3 particles shows that these particles are aspherical and their ρ_e are independent of particle size. Coupled with the ability of SPAMS to characterize the chemical composition of individual particles, the AAC-SPAMS system is demonstrated to be capable of characterizing the D_{ve} , $\rho_e(\rho_p/\chi)$ and chemical compositions of atmospheric particles simultaneously, showing the potential application of this system in field observations. The approach achieves the measurement of chemically resolved D_{ve} and $\rho_e(\rho_p/\chi)$ and provides the possibility to determine their quantitative relationship with other particle properties, which would be a benefit for further reduction of the uncertainty associated with the effects of particles on air quality, human health, and radiative forcing.

Data availability. Data in this study are available at <https://doi.org/10.5281/zenodo.4655206> (Peng, 2021).

Supplement. The supplement related to this article is available online at: <https://doi.org/10.5194/acp-21-5605-2021-supplement>.

Author contributions. The idea for the study was conceived by LP and GHZ. All experiments were performed by LP with the assistance of LL. LP wrote the paper, which was reviewed by GHZ and XHB. All co-authors discussed the results and commented on the manuscript.

Competing interests. The authors declare that they have no conflict of interest.

Acknowledgements. The authors gratefully acknowledge Cambustion Ltd., UK, for providing the AAC and Hexin Analytical Instrument Co., Ltd., China, for providing the SPAMS. This is contribution no. IS-2995 from CASGIG.

Financial support. This research has been supported by the National Nature Science Foundation of China (grant nos. 41877307 and 41775124), the Natural Science Foundation of Guangdong Province (grant no. 2019B151502022), and the Guangdong Foundation for the Program of Science and Technology Research (grant nos. 2019B121205006 and 2020B1212060053).

Review statement. This paper was edited by James Allan and reviewed by Johannes Schneider and one anonymous referee.

References

- Alexander, J. M., Bell, D. M., Imre, D., Kleiber, P. D., Grassian, V. H., and Zelenyuk, A.: Measurement of size-dependent dynamic shape factors of quartz particles in two flow regimes, *Aerosol Sci. Tech.*, 50, 870–879, <https://doi.org/10.1080/02786826.2016.1200006>, 2016.
- Beranek, J., Imre, D., and Zelenyuk, A.: Real-time shape-based particle separation and detailed in situ particle shape characterization, *Anal. Chem.*, 84, 1459–1465, <https://doi.org/10.1021/ac202235z>, 2012.
- Buseck, P. R. and Posfai, M.: Airborne minerals and related aerosol particles: effects on climate and the environment, *P. Natl. Acad. Sci. USA*, 96, 3372–3379, <https://doi.org/10.1073/pnas.96.7.3372>, 1999.
- Cross, E. S., Slowik, J. G., Davidovits, P., Allan, J. D., Worsnop, D. R., Jayne, J. T., Lewis, D. K., Canagaratna, M., and Onasch, T. B.: Laboratory and ambient particle density determinations using light scattering in conjunction with aerosol mass spectrometry, *Aerosol Sci. Tech.*, 41, 343–359, <https://doi.org/10.1080/02786820701199736>, 2007.
- DeCarlo, P. F., Slowik, J. G., Worsnop, D. R., Davidovits, P., and Jimenez, J. L.: Particle morphology and density characterization by combined mobility and aerodynamic diameter measurements. Part 1: Theory, *Aerosol Sci. Tech.*, 38, 1185–1205, <https://doi.org/10.1080/027868290903907>, 2004.
- Dinar, E., Mentel, T. F., and Rudich, Y.: The density of humic acids and humic like substances (HULIS) from fresh and aged wood burning and pollution aerosol particles, *Atmos. Chem. Phys.*, 6, 5213–5224, <https://doi.org/10.5194/acp-6-5213-2006>, 2006.
- Guo, S., Hu, M., Zamora, M. L., Peng, J. F., Shang, D. J., Zheng, J., Du, Z. F., Wu, Z., Shao, M., Zeng, L. M., Molina, M. J., and Zhang, R. Y.: Elucidating severe urban haze formation in China, *P. Natl. Acad. Sci. USA*, 111, 17373–17378, 2014.
- Han, C., Li, S. M., Liu, P., and Lee, P.: Size dependence of the physical characteristics of particles containing refractory black carbon in diesel vehicle exhaust, *Environ. Sci. Technol.*, 53, 137–145, <https://doi.org/10.1021/acs.est.8b04603>, 2019.
- Hand, J. L. and Kreidenweis, S. M.: A new method for retrieving particle refractive index and effective density from aerosol size distribution data, *Aerosol Sci. Tech.*, 36, 1012–1026, <https://doi.org/10.1080/02786820290092276>, 2002.
- Hoffman, R. C., Laskin, A., and Finlayson-Pitts, B. J.: Sodium nitrate particles: physical and chemical properties during hydration and dehydration, and implications for aged sea salt aerosols, *J. Aerosol Sci.*, 35, 869–887, 2004.
- Katrib, Y., Martin, S. T., Rudich, Y., Davidovits, P., Jayne, J. T., and Worsnop, D. R.: Density changes of aerosol particles as a result of chemical reaction, *Atmos. Chem. Phys.*, 5, 275–291, <https://doi.org/10.5194/acp-5-275-2005>, 2005.
- Kiselev, A., Wennrich, C., Stratmann, F., Wex, H., Henning, S., Mentel, T. F., Kiendler-Scharr, A., Schneider, J., Walter, S., and Lieberwirth, I.: Morphological characterization of soot aerosol particles during LACIS Experiment in November (LEXNo), *J. Geophys. Res.-Atmos.*, 115, D11204, <https://doi.org/10.1029/2009jd012635>, 2010.
- Li, L., Huang, Z. X., Dong, J. G., Li, M., Gao, W., Nian, H. Q., Fu, Z., Zhang, G. H., Bi, X. H., Cheng, P., and Zhou, Z.: Real time bipolar time-of-flight mass spectrometer for analyzing single aerosol particles, *Int. J. Mass Spectrom.*, 303, 118–124, <https://doi.org/10.1016/j.ijms.2011.01.017>, 2011.
- Liu, Y. and Daum, P. H.: Relationship of refractive index to mass density and self-consistency of mixing rules for multicomponent mixtures like ambient aerosols, *J. Aerosol Sci.*, 39, 974–986, <https://doi.org/10.1016/j.jaerosci.2008.06.006>, 2008.
- Liu, Z., Hu, B., Ji, D., Wang, Y., Wang, M., and Wang, Y.: Diurnal and seasonal variation of the PM_{2.5} apparent particle density in Beijing, China, *Atmos. Environ.*, 120, 328–338, <https://doi.org/10.1016/j.atmosenv.2015.09.005>, 2015.
- Moffet, R. C. and Prather, K. A.: Extending ATOFMS measurements to include refractive index and density, *Anal. Chem.*, 77, 6535–6541, <https://doi.org/10.1021/ac0503097>, 2005.
- Moffet, R. C., Qin, X., Rebotier, T., Furutani, H., and Prather, K. A.: Chemically segregated optical and microphysical properties of ambient aerosols measured in a single-particle mass spectrometer, *J. Geophys. Res.-Atmos.*, 113, D12213, <https://doi.org/10.1029/2007jd009393>, 2008.
- Peng, J. F., Hu, M., Guo, S., Du, Z. F., Zheng, J., Shang, D. J., Zamora, M., Zeng, L. M., Shao, M., Wu, Y. S., Zheng, J., Wang, Y., Glen, C., Collins, D., Molina, M., and Zhang, R. Y.: Markedly enhanced absorption and direct radiative forcing of black carbon under polluted urban environments, *P. Natl. Acad. Sci. USA*, 113, 4266–4271, <https://doi.org/10.1073/pnas.1602310113>, 2016.
- Peng, L.: longer1217/All-figures-data: Data (Version V1), Zenodo, <https://doi.org/10.5281/zenodo.4655206>, 2021.
- Peng, L. and Bi, X.: Comment on “Retrieval of atmospheric fine particulate density based on merging particle size distribution measurements: multi-instrument observation and quality control at Shouxian” by Li et al, *J. Geophys. Res.-Atmos.*, 125, e2019JD031806, <https://doi.org/10.1029/2019JD031806>, 2020.
- Pitz, M., Cyrus, J., Karg, E., Wiedensohler, A., Wichmann, H. E., and Heinrich, J.: Variability of apparent particle density of an urban aerosol, *Environ. Sci. Technol.*, 37, 4336–4342, <https://doi.org/10.1021/es034322p>, 2003.
- Pöschl, U.: Atmospheric aerosols: Composition, transformation, climate and health effects, *Angew. Chem. Int. Edit.*, 44, 7520–7540, <https://doi.org/10.1002/anie.200501122>, 2005.
- Schneider, J., Weimer, S., Drewnick, F., Borrmann, S., Helas, G., Gwaze, P., Schmid, O., Andreae, M. O., and Kirchner, U.: Mass spectrometric analysis and aerodynamic properties of various types of combustion-related aerosol particles, *Int. J. Mass Spectrom.*, 258, 37–49, <https://doi.org/10.1016/j.ijms.2006.07.008>, 2006.
- Seinfeld, J. and Pandis, S. N.: From air pollution to climate change, *Atmospheric Chemistry and Physics*, Wiley, New York, 429–443, 1998.
- Song, X. H., Hopke, P. K., Fergenson, D. P., and Prather, K. A.: Classification of single particles analyzed by ATOFMS using an artificial neural network, ART-2A, *Anal. Chem.*, 71, 860–865, <https://doi.org/10.1021/ac9809682>, 1999.
- Spencer, M. T. and Prather, K. A.: Using ATOFMS to determine OC/EC mass fractions in particles, *Aerosol Sci. Tech.*, 40, 585–594, <https://doi.org/10.1080/02786820600729138>, 2006.

- Spencer, M. T., Shields, L. G., and Prather, K. A.: Simultaneous measurement of the effective density and chemical composition of ambient aerosol particles, *Environ. Sci. Technol.*, 41, 1303–1309, <https://doi.org/10.1021/es061425+>, 2007.
- Sumlin, B. J., Oxford, C. R., Seo, B., Pattison, R. R., Williams, B. J., and Chakrabarty, R. K.: Density and homogeneous internal composition of primary brown carbon Aerosol, *Environ. Sci. Technol.*, 52, 3982–3989, <https://doi.org/10.1021/acs.est.8b00093>, 2018.
- Tang, I. N.: Thermodynamic and optical properties of mixed-salt aerosols of atmospheric importance, *J. Geophys. Res.-Atmos.*, 102, 1883–1893, 1997.
- Tang, I. N. and Munkelwitz, H. R.: Water activities, densities, and refractive-indexes of aqueous sulfates and sodium-nitrate droplets of atmospheric importance, *J. Geophys. Res.-Atmos.*, 99, 18801–18808, 1994.
- Tavakoli, F. and Olfert, J. S.: An instrument for the classification of aerosols by particle relaxation time: theoretical models of the aerodynamic aerosol classifier, *Aerosol Sci. Tech.*, 47, 916–926, <https://doi.org/10.1080/02786826.2013.802761>, 2013.
- Wu, Y., Xia, Y., Huang, R., Deng, Z., Tian, P., Xia, X., and Zhang, R.: A study of the morphology and effective density of externally mixed black carbon aerosols in ambient air using a size-resolved single-particle soot photometer (SP2), *Atmos. Meas. Tech.*, 12, 4347–4359, <https://doi.org/10.5194/amt-12-4347-2019>, 2019.
- Yin, Z., Ye, X. N., Jiang, S. Q., Tao, Y., Shi, Y., Yang, X., and Chen, J. M.: Size-resolved effective density of urban aerosols in Shanghai, *Atmos. Environ.*, 100, 133–140, <https://doi.org/10.1016/j.atmosenv.2014.10.055>, 2015.
- Yon, J., Bescond, A., and Ouf, F. X.: A simple semi-empirical model for effective density measurements of fractal aggregates, *J. Aerosol Sci.*, 87, 28–37, <https://doi.org/10.1016/j.jaerosci.2015.05.003>, 2015.
- Zelenyuk, A., Cai, Y., Chieffo, L., and Imre, D.: High precision density measurements of single particles: The density of metastable phases, *Aerosol Sci. Tech.*, 39, 972–986, <https://doi.org/10.1080/02786820500380206>, 2005.
- Zelenyuk, A., Cai, Y., and Imre, D.: From agglomerates of spheres to irregularly shaped particles: Determination of dynamic shape factors from measurements of mobility and vacuum aerodynamic diameters, *Aerosol Sci. Tech.*, 40, 197–217, <https://doi.org/10.1080/02786820500529406>, 2006.
- Zhai, J., Lu, X., Li, L., Zhang, Q., Zhang, C., Chen, H., Yang, X., and Chen, J.: Size-resolved chemical composition, effective density, and optical properties of biomass burning particles, *Atmos. Chem. Phys.*, 17, 7481–7493, <https://doi.org/10.5194/acp-17-7481-2017>, 2017.
- Zhang, G., Bi, X., Han, B., Qiu, N., Dai, S., Wang, X., Sheng, G., and Fu, J.: Measurement of aerosol effective density by single particle mass spectrometry, *Sci. China Earth Sci.*, 59, 320–327, <https://doi.org/10.1007/s11430-015-5146-y>, 2016.
- Zhang, Y., Zhang, Q., Cheng, Y., Su, H., Kecorius, S., Wang, Z., Wu, Z., Hu, M., Zhu, T., Wiedensohler, A., and He, K.: Measuring the morphology and density of internally mixed black carbon with SP2 and VTDMA: new insight into the absorption enhancement of black carbon in the atmosphere, *Atmos. Meas. Tech.*, 9, 1833–1843, <https://doi.org/10.5194/amt-9-1833-2016>, 2016.
- Zhao, G., Zhao, W., and Zhao, C.: Method to measure the size-resolved real part of aerosol refractive index using differential mobility analyzer in tandem with single-particle soot photometer, *Atmos. Meas. Tech.*, 12, 3541–3550, <https://doi.org/10.5194/amt-12-3541-2019>, 2019.